



The AOTF-based NO₂ camera

Emmanuel Dekemper¹, Jurgen Vanhamel¹, Bert Van Opstal¹, and Didier Fussen¹

¹Royal Belgian Institute for Space Aeronomy, avenue Circulaire 3, 1180 Brussels, Belgium

Correspondence to: E. Dekemper (emmanuel.dekemper@aeronomie.be)

Abstract. The abundance of NO₂ in the boundary layer relates to air quality and pollution sources monitoring. Observing the spatio-temporal distribution of NO₂ above well-delimited (flue gas stacks, volcanoes, ships) or more extended sources (cities) allows for several applications: monitoring emission fluxes or studying the plume dynamic chemistry and its transport. So far, most attempts to map the NO₂ field from the ground have been made with visible-light scanning spectrometers. Benefiting from a high retrieval accuracy, they only achieve a relatively low temporal resolution that hampers the detection of dynamic features.

We present a new type of passive remote sensing instrument aiming at the measurement of the 2-D distributions of NO₂ slant column densities (SCD) with a high spatio-temporal resolution. The measurement principle has strong similarities with the popular filter-based SO₂ camera as it relies on spectral images taken at wavelengths where the molecule absorption cross-section is different. Contrary to the SO₂ camera, the spectral selection is performed by an acousto-optical tunable filter (AOTF) capable of resolving the target molecule's spectral features.

The NO₂ camera capabilities are demonstrated by imaging the NO₂ abundance in the plume of a coal-fired power plant. During this experiment, the 2-D distribution of the NO₂ SCD was retrieved with a temporal resolution of 3 minutes and a spatial sampling of 50 cm (over a 250 × 250 m² area). The detection limit was close to 5 × 10¹⁶ molecules cm⁻², with a maximum detected SCD of 4 × 10¹⁷ molecules cm⁻². Illustrating the added-value of the NO₂ camera measurements, the data reveal the dynamics of the NO to NO₂ conversion in the early plume with an unprecedented resolution: from its release in the air, and for 100 m upwards, the observed NO₂ plume concentration increased at a rate of 0.75-1.25 g s⁻¹. In joint campaigns with SO₂ cameras, the NO₂ camera could also help in removing the bias introduced by the NO₂ interference in the SO₂ measurements.

1 Introduction

Nitrogen oxides (NO_x=NO + NO₂) play a key role in the air quality of the boundary layer. While NO is produced in combustion processes (transport, thermal power plants, etc.), NO₂ mainly appears through the reaction of NO with O₃ or HO₂. Eventually, the photolysis of NO₂ releases an oxygen atom and a NO molecule. To a good approximation, the balance of NO and NO₂ is kept constant through this cycle of photo-chemical reactions, which substantiates the widespread use of the NO_x family concept (Seinfeld and Pandis, 2006). Considering the relative ease of measuring NO₂ with visible-light spectroscopy, NO_x budgets are often inferred based on NO₂ measurements and the photochemical equilibrium assumption.



The most common NO₂ remote sensing techniques rely on the differential optical absorption spectroscopy (DOAS), which is based on the fitting of radiance spectra with the effective absorption cross-section of interfering species (e.g. Lohberger et al., 2004). If equipped with a 2-D sensor array, these instruments disperse the light spectrum along one dimension and record its spatial variation along the other. Building a complete hyperspectral image requires an incremental depointing of the instantaneous field of view (FOV), or a translation of the whole instrument. Typical examples of both applications can be found in Heue et al. (2008) or Lohberger et al. (2004). While the DOAS technique is well validated in terms of accuracy and sensitivity, the need for scanning the scene hampers the detection of dynamic processes. As the scene is sampled slice by slice, the final image does not show a great temporal consistency: different rows (or columns depending on the scanning direction) are temporally disconnected from each other. The time gap can reach several minutes between both edges of the scene.

There are situations where high spatio-temporal resolution is needed. In volcanology for instance, the main measurement technique for the SO₂ released in volcanic plumes has recently moved from spectrometers (gas-correlation or DOAS methods) to so-called SO₂ cameras (Mori and Burton, 2006; Bluth et al., 2007), although infrared imagers have also been developed (see Platt et al. (2014) for a review of techniques). Their concept is based on taking spectral images of the plume through two interference filters. One filter selects a narrow band of the incident spectrum around 310 nm where SO₂ is still strongly absorbing, the other one captures the light around 330 nm where almost no more absorption takes place. The main advantages are a typical temporal resolution of 1 Hz, the capability to capture dynamic features such as puffs in the plume, and the possibility to determine the plume speed from the sequence of images. The disadvantages are the interference by the plume aerosols caused by the coarse spectral resolution, and the need for regular re-calibration with reference cells filled with SO₂ to account for changes of illumination conditions (Kern et al., 2010). More recent concepts now use the combined information of a spectrometer with the camera spectral images (Lübcke et al., 2013) which yields a greater measurement accuracy.

We present a new instrument, a spectral imager dedicated to measuring the 2-D NO₂ field above finite sources like thermal power plants, industrial complexes, cities, volcanoes, ... The measurement principle is close to the SO₂ camera: snapshots at two wavelengths emphasize the presence of NO₂ by taking advantage of absolute differences in the molecule absorption cross section. Contrary to the SO₂ cameras which use interference filters, the new instrument relies on an acousto-optical tunable filter (AOTF) to provide the spectral information. The AOTF can offer sufficient spectral resolution to resolve the structures of the NO₂ spectrum. The ability to discriminate between weak and strong absorption within a few nanometres virtually cuts out any sensitivity to aerosol scattering and changes of solar angles. Potential applications tackle urban and industrial pollution monitoring, emission fluxes estimation, satellite-products validation, volcanic plume chemistry.

2 Instrument concept

The AOTF-based NO₂ camera derives from the ALTIUS instrument (atmospheric limb tracker for the investigation of the upcoming stratosphere). ALTIUS is a space mission project aiming at the retrieval of atmospheric constituents densities with a global geographical coverage and a high vertical resolution. Its primary scientific objective is to measure ozone, but NO₂, aerosols, H₂O, CH₄, polar stratospheric and noctilucent clouds, and other minor species will be measured as well. Measure-

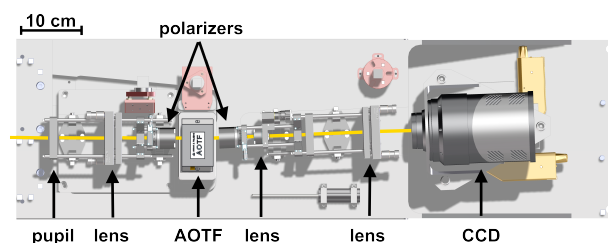


Figure 1. Optical layout of the NO₂ camera seen from top. Light propagates from left to right through a pupil and a lens doublet, a polarizer selecting vertically-polarized light, the AOTF, a second cross-oriented polarizer, two lens doublets and the detector.

ments will be performed in two different geometries: limb scattering and occultations (Sun, Moon, stars, planets). To address the problem of tangent height registration of previous limb scatter instruments, a spectral imager concept based on a tunable filter has been selected. During the feasibility study, an optical breadboard of the visible (VIS) channel (440-800 nm) was built from commercially-available parts. The detailed description of this breadboard is given in Dekemper et al. (2012). We will only point out the key features of the concept.

The instrument offers a 6° square FOV imaging onto a Princeton Instrument Pixis 512B peltier-cooled CCD detector (512 × 512 pixels). The optical layout (Fig. 1) is linear with an intermediate focal plane located close to the AOTF. To preserve the spectral homogeneity across the image, the design is made telecentric by placing an iris at the object focal point of the first lens. This ensures an identical propagation angle of all light rays through the AOTF.

The most important part of this NO₂ camera concept is the AOTF (Chang, 1974). AOTFs have been used in many areas requiring spectral images (agriculture, food industry, fluorescence spectroscopy, etc), but received little attention from the atmospheric remote sensing community. The working principle is based on the interaction of light and sound in a birefringent crystal (see Fig. 2). By the momentum matching of the optical and acoustic waves, a narrow portion of the light spectrum is diffracted into a slightly different direction (a few degrees). If the incident radiation is linearly polarized, the diffracted beam will leave the crystal with the orthogonal polarization. The spatial and polarimetric dissociations can be combined to achieve very efficient extinction of the unwanted spectrum.

The wave vectors matching condition creates a monotonic relationship between the light wavelength and the sound frequency. The acoustic wave is launched into the crystal by a piezoelectric transducer bonded to one of its facets. Hence, selecting a particular wavelength λ simply requires to drive the transducer to the matching frequency $F(\lambda)$. The AOTF spectral transmission function (STF) closely follows a sinc^2 shape. The amplitude of the STF, which determines the filter diffraction efficiency (DE), is controlled by the acoustic power $P_a(\lambda)$ which also exhibits a smooth wavelength dependence. The transducer length defines the length of the acousto-optic interaction which directly affects the AOTF bandwidth: a short transducer will induce a larger passband and vice-versa.

The parameters of an AOTF are defined by the crystal elastic and optical properties, and by the propagation directions of light and sound in the frame of the crystal axes (Voloshinov et al., 2007). The AOTF we used was manufactured out of a

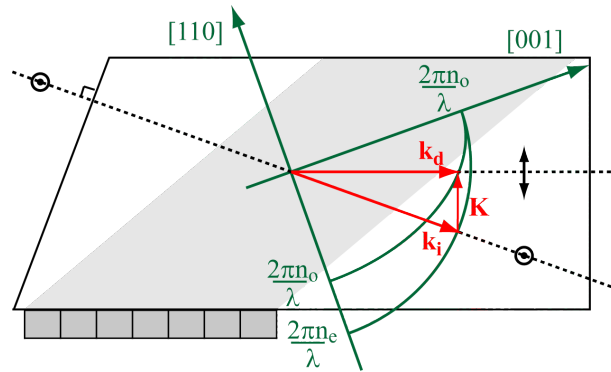


Figure 2. Schematics of the acousto-optic interaction in an AOTF (top view). The gray area depicts the acoustic field created by the piezo-electric transducer bonded to a lateral face of the TeO_2 crystal. The momentum phase matching of the incident (\mathbf{k}_i) and diffracted (\mathbf{k}_d) photons with the acoustic wave (\mathbf{K}) is represented in the $[\bar{1}10]$ crystallographic frame. The phase matching takes advantage of the medium birefringence: incident and diffracted light beams have orthogonal polarisations and different propagation directions which facilitates their selection.

TeO_2 crystal by the company Gooch & Housego (U.K.). It offers an aperture of $10 \times 10 \text{ mm}^2$, and a tuning range covering the visible spectrum. Laboratory characterization revealed a transparency better than 90%, and a DE better than 95%. In the relevant spectral range for NO_2 measurements, i.e. around 450 nm, the STF showed a bandwidth of 0.6 nm. Typical driving frequencies were around 130 MHz, and less than 100 mW of acoustic power was needed in any circumstances. The theoretical number of resolvable spots at 450 nm is about 350 in the plane of acousto-optic interaction (horizontal axis), and 700 in the vertical direction.

3 Measurement principle

There are strong similarities between the measurement principles of a filter-based SO_2 camera and an AOTF-based NO_2 camera: the FOV needs to be pointed towards the target region (e.g. a plume) while making sure that the background can still be seen in some areas of the image. Two spectral images of the scene are taken: one at a wavelength λ_s where there is strong absorption by the target species, another at a wavelength λ_w where there is weak absorption. In each image, the signal $S_{ij}(\lambda)$ (in e^-) recorded by pixel ij looking at the plume will be normalized by the background signal $S_0(\lambda)$ in order to emphasize the extinction that took place during the crossing of the plume. The optical thickness τ_{ij} associated with the slant column density (SCD) of the target species observed in the FOV of pixel ij follows from the comparison of the normalized signals recorded at the two wavelengths.

The major difference comes from the capability of the AOTF-based NO_2 camera to resolve the fine structures of the absorption cross section σ_{NO_2} (Fig. 3). This allows choosing λ_s and λ_w very close to each other (a few nm), minimizing the interference by broadband absorbing and scattering species like aerosols.

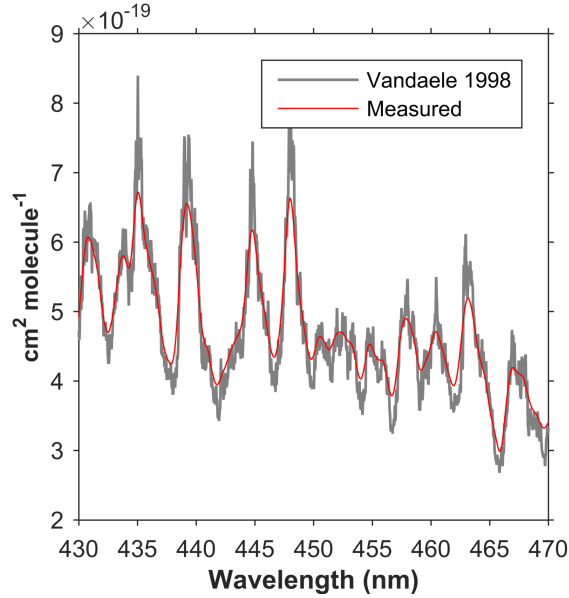


Figure 3. NO₂ absorption cross section measured with a fourier transform spectrometer (gray line, (Vandaele et al., 1998)), and with this NO₂ camera in the laboratory (red line). At 450 nm, the spectral resolution of both datasets are 0.04 nm and 0.6 nm respectively.

3.1 Mathematical model

As AOTFs do not treat different polarizations identically, an AOTF-based NO₂ camera exhibits a strong polarization sensitivity. The polarization state of a stream of light is described by the Stokes vector $s = (I, Q, U, V)^T$, where $I = I^h + I^v$ and $Q = I^h - I^v$ with I^h and I^v being the light intensity along the horizontal and vertical axes of a scene frame. U and V also refer to the orientation of the polarization ellipse but they will not be discussed further because they do not participate if the AOTF and its surrounding polarizers are well aligned.

When light passes through a polarizing part, its Stokes vector can be changed. A polarizing element is therefore represented by a 4×4 transfer matrix: the Mueller matrix M . A chain of optical elements is represented by the product of their Mueller matrices. In our design, the light passes first through a vertical linear polarizer, then the AOTF, and finally a horizontal linear polarizer. The Stokes vector representing the light leaving the second polarizer is therefore given by $s' = M_{Ph} \cdot M_{AOTF} \cdot M_{Pv} \cdot s$. The Mueller matrices of the elements are as follows:

$$M_{AOTF} = \frac{A}{2} \begin{pmatrix} 1 & -1 & 0 & 0 \\ 1 & -1 & 0 & 0 \\ 0 & 0 & 0 & 0 \\ 0 & 0 & 0 & 0 \end{pmatrix}, \quad (1)$$



$$\mathbf{M}_{\text{Pv}} = \frac{1}{2} \begin{pmatrix} \eta_e^2 + \eta_t^2 & \eta_e^2 - \eta_t^2 & 0 & 0 \\ \eta_e^2 - \eta_t^2 & \eta_e^2 + \eta_t^2 & 0 & 0 \\ 0 & 0 & 2\eta_e\eta_t & 0 \\ 0 & 0 & 0 & 2\eta_e\eta_t \end{pmatrix}, \quad \mathbf{M}_{\text{Ph}} = \frac{1}{2} \begin{pmatrix} \eta_t^2 + \eta_e^2 & \eta_t^2 - \eta_e^2 & 0 & 0 \\ \eta_t^2 - \eta_e^2 & \eta_t^2 + \eta_e^2 & 0 & 0 \\ 0 & 0 & 2\eta_e\eta_t & 0 \\ 0 & 0 & 0 & 2\eta_e\eta_t \end{pmatrix}, \quad (2)$$

where A is the amplitude of the AOTF STF (i.e. its DE, $0 \leq A \leq 1$), η_t^2 is the attenuation of the light intensity along the polarizer transmission axis, and η_e^2 does the same for the extinction axis. Assuming that all three elements have their transmission and extinction axes well aligned, the total Mueller matrix of the camera is simply $\mathbf{M} = \eta_t^4 \cdot \mathbf{M}_{\text{AOTF}}$. As the detector only measures the total light intensity, the first element of the Stokes vector is the only meaningful quantity: $s'(1) = A \cdot \eta_t^4 \cdot (I - Q)/2 = A \cdot \eta_t^4 \cdot I^v$. Hence, in the present configuration, the NO₂ camera is only sensitive to vertically polarized light.

We now have a description of the light intensity which will be measured by the detector, but we still have to account for the extinction by the lenses (T) and the quantum efficiency (QE) of the detector. These terms exhibit a smooth wavelength dependence. For the AOTF STF, one can use $\mathcal{F}(\lambda; \lambda_c) = A(\lambda_c) \cdot G(\lambda - \lambda_c)$, where G is essentially a sinc² function. Moreover, some parameters are susceptible to vary across the FOV, yielding a pixel-to-pixel variation. This is particularly true when image planes are located close to optical surfaces (mainly the AOTF and the detector). Finally, the electronic current (in e⁻s⁻¹) found in pixel ij when the AOTF is tuned to λ_c is given by:

$$\begin{aligned} C_{ij}(\lambda_c) &= \int A_{ij}(\lambda_c) \cdot \eta_t^4(\lambda) \cdot I_{ij}^v(\lambda) \cdot G(\lambda - \lambda_c) \cdot T(\lambda) \cdot \text{QE}_{ij}(\lambda) d\lambda, \\ &= A_{ij}(\lambda_c) \cdot \eta_t^4(\lambda_c) \cdot T(\lambda_c) \cdot \text{QE}_{ij}(\lambda_c) \int I_{ij}^v(\lambda) \cdot G(\lambda - \lambda_c) d\lambda, \\ &= r_{ij}(\lambda_c) \int I_{ij}^v(\lambda) \cdot G(\lambda - \lambda_c) d\lambda. \end{aligned} \quad (3)$$

The decision to leave the smoothly varying parameters out of the integral is supported by the narrow passband of the AOTF (0.6 nm). Their product forms the instrument response at pixel ij and wavelength λ_c : $r_{ij}(\lambda_c)$. The remaining integral is simply the convolution of the vertically-polarized incident light intensity with the AOTF STF.

Suppose now that pixel ij is looking through an optically thin plume. NO₂ and other species will absorb or scatter photons and decrease the background light intensity I_0^v according to the Beer-Lambert law of extinction:

$$I_{ij}^v(\lambda) = I_0^v(\lambda) \cdot \exp\left(-\tau_{\text{NO}_2, ij}(\lambda) - \tau_{\star, ij}(\lambda)\right), \quad (4)$$

where $\tau_{\text{NO}_2, ij}$ denotes the plume optical thickness caused by absorption by NO₂ along the light path reaching of pixel ij , and $\tau_{\star, ij}$ is the effective optical thickness of all other chemical species and particles. Over the passband of the AOTF, one can consider $\tau_{\star}(\lambda)$ as a constant value $\tau_{\star}(\lambda_c)$ and replace $\tau_{\text{NO}_2}(\lambda)$ by its weighted average:

$$\bar{\tau}_{\text{NO}_2}(\lambda_c) = \frac{\int \tau_{\text{NO}_2}(\lambda) \cdot G(\lambda - \lambda_c) d\lambda}{\int G(\lambda - \lambda_c) d\lambda}.$$

As the optical thickness is defined by the product of the trace gas SCD k with its absorption cross-section σ , it is clear that $\bar{\tau}_{\text{NO}_2}(\lambda_c) = k_{\text{NO}_2} \cdot \bar{\sigma}_{\text{NO}_2}(\lambda_c)$. Under these assumptions, one can replace Eq. (4) into Eq. (3) and write for the pixel photoelectric



current:

$$C_{ij}(\lambda_c) = r_{ij}(\lambda_c) \cdot \exp\left(-\bar{\tau}_{\text{NO}_2\ ij}(\lambda_c) - \tau_{\star\ ij}(\lambda_c)\right) \cdot \int I_0^v(\lambda) \cdot G(\lambda - \lambda_c) d\lambda. \quad (5)$$

In the meantime, other pixels have been looking at the unattenuated background intensity I_0 . Suppose that one of them is pixel mn . According to Eq. (3), we have:

$$C_{mn}(\lambda_c) = r_{mn}(\lambda_c) \cdot \int I_0^v(\lambda) \cdot G(\lambda - \lambda_c) d\lambda.$$

Averaging all these background-looking pixels yields the reference current associated with the background intensity:

$$C_0(\lambda_c) = r(\lambda_c) \cdot \int I_0^v(\lambda) \cdot G(\lambda - \lambda_c) d\lambda, \quad (6)$$

- 5 with r representing the average instrument response. Dividing C_{ij} by C_0 yields the transmittance of the plume only:

$$T_{ij}(\lambda_c) = \frac{\frac{C_{ij}(\lambda_c)}{r_{ij}(\lambda_c)}}{\frac{C_0(\lambda_c)}{r(\lambda_c)}} = \exp\left(-\bar{\tau}_{\text{NO}_2\ ij}(\lambda_c) - \tau_{\star\ ij}(\lambda_c)\right). \quad (7)$$

If the plume transmittance is calculated for each of the two carefully-selected wavelengths λ_w and λ_s , then it is possible to cancel the interference of other species (because $\tau_{\star}(\lambda_w) = \tau_{\star}(\lambda_s)$ if λ_w and λ_s are very close). Introducing the relative instrument response at pixel ij : $\rho_{ij}(\lambda) = r_{ij}(\lambda)/r(\lambda)$, the ratio of transmittances

$$\frac{T_{ij}(\lambda_w)}{T_{ij}(\lambda_s)} = \frac{\frac{C_{ij}(\lambda_w)}{C_0(\lambda_w)\rho_{ij}(\lambda_w)}}{\frac{C_{ij}(\lambda_s)}{C_0(\lambda_s)\rho_{ij}(\lambda_s)}} = \exp\left(\bar{\tau}_{\text{NO}_2\ ij}(\lambda_s) - \bar{\tau}_{\text{NO}_2\ ij}(\lambda_w)\right), \quad (8)$$

which yields the NO_2 SCD observed by pixel ij :

$$k_{\text{NO}_2\ ij} = \frac{1}{\bar{\sigma}_{\text{NO}_2}(\lambda_s) - \bar{\sigma}_{\text{NO}_2}(\lambda_w)} \cdot \ln\left(\frac{T_{ij}(\lambda_w)}{T_{ij}(\lambda_s)}\right). \quad (9)$$

10 3.2 Ancillary data

Equation (9) shows that the NO_2 SCD can be obtained from a combination of measurements (the detector signal), cross-section data and the knowledge of the instrument response. In the results presented below, the cross-section is taken from Vandaele et al. (1998). For the ρ_{ij} coefficients, an *ad hoc* method was set up to build a synthetic flat field. Taking advantage of a cloudy weather (100% cloudiness), long-exposure frames (10 s) were captured at the required wavelengths looking at zenith. The mean image obtained from tens of such frames constitutes the instrument response to a synthetic, radiometrically flat, scene. This allows to remove wavelength-dependent non-uniformities which can be relatively pronounced in the AOTF for instance.

- Access to the photoelectric current strictly proportional to the signal (i.e. C_{ij} and C_0) implies that voltage offset, dark current and stray light have been subtracted from the raw data. In this respect, AOTFs offer a unique feature: one can turn them off. This is simply done by setting the RF level to 0. An image acquired in these conditions contains anything but the real signal (i.e. dark current, offset, straylight). Using D_{ij} and D_{ij}^{off} to represent the raw signal of pixel ij (in digital numbers, DN) when the AOTF is turned on or off respectively, the photo-electric signal is given by

$$S_{ij} = \frac{D_{ij} - D_{ij}^{\text{off}}}{G}, \quad (10)$$



where G is the sensor gain (in DN/e⁻). The only precaution is to take these dark images regularly because, the straylight being connected with the general illumination conditions (e.g. solar angles), it will vary with time.

3.3 Data averaging and multiple image doublets

It is often necessary to repeat the measurements in order to average out transient features and increase the signal-to-noise ratio (SNR). Assuming that only the plume optical transmission varies, we can write a time-dependent version of Eq. (5):

$$C_{ij}(\lambda_c, t) = r_{ij}(\lambda_c) \cdot \exp\left(-\bar{\tau}_{\text{NO}_2, ij}(\lambda_c, t) - \tau_{\star, ij}(\lambda_c, t)\right) \cdot \int I_0^v(\lambda) \cdot G(\lambda - \lambda_c) d\lambda. \quad (11)$$

The time-averaged optical thickness $\tau(\lambda, \bar{t})$ can be obtained from the geometric mean of the consecutive images:

$$\begin{aligned} \sqrt[N]{\prod_{k=1}^N C_{ij}(\lambda_c, t_k)} &= r_{ij}(\lambda_c) \cdot \exp\left(-\frac{1}{N} \sum_{k=1}^N \bar{\tau}_{\text{NO}_2, ij}(\lambda_c, t_k) + \tau_{\star, ij}(\lambda_c, t_k)\right) \cdot \int I_0^v(\lambda) \cdot G(\lambda - \lambda_c) d\lambda. \\ &= r_{ij}(\lambda_c) \cdot \exp\left(-\bar{\tau}_{\text{NO}_2, ij}(\lambda_c, \bar{t}) - \tau_{\star, ij}(\lambda_c, \bar{t})\right) \cdot \int I_0^v(\lambda) \cdot G(\lambda - \lambda_c) d\lambda. \end{aligned} \quad (12)$$

Another means of increasing the reliability of the measurements is to use different doublets, i.e. pairs of λ_w and λ_s . If the transmittance is known for several doublets, their product strengthens the NO₂ SCD retrieval by providing information from multiple spectral regions. If $\Delta\sigma_{\text{NO}_2} = \bar{\sigma}_{\text{NO}_2}(\lambda_s) - \bar{\sigma}_{\text{NO}_2}(\lambda_w)$, then for two doublets, we have for the SCD:

$$k_{\text{NO}_2, ij} = \frac{1}{\Delta\sigma_{\text{NO}_2}^{(1)} + \Delta\sigma_{\text{NO}_2}^{(2)}} \cdot \ln\left(\frac{T_{ij}(\lambda_{w1}) \cdot T_{ij}(\lambda_{w2})}{T_{ij}(\lambda_{s1}) \cdot T_{ij}(\lambda_{s2})}\right). \quad (13)$$

10 This approach can potentially attenuate a bias in one of the measurements.

3.4 Error budget and instrument sensitivity

Obviously, one can work out Eq. (5) with the classical first-order Taylor expansion approximation to determine the uncertainty on the NO₂ SCD. This approach will require estimates of the uncertainty on the photon counts C_{ij} , on the background signal C_0 , on the relative instrument response ρ_{ij} , and on the cross-section data σ_{NO_2} . These estimates are not always easily obtained, and we briefly discuss each of them.

The photo-electric counting rates C_{ij} are obtained from Eq. (10): $C_{ij} = S_{ij}/t$, where t is the sensor exposure time. It is reasonable to assume that the camera operator selected acquisition settings ensuring that the signal is well into the shot noise regime: $\sigma_{C_{ij}} = \sqrt{S_{ij}}/t$. With signals exceeding 10⁴ e⁻ in 1 second (the case in the examples below), the relative uncertainty on C_{ij} will be below 1%.

20 The background signal C_0 is estimated by averaging the pixels looking at the background of the scene. While one would presume that the averaging of a large number of such pixels should yield a very high precision, the efficiency is limited by the difficulty to identify pixels effectively looking at the background. Automated data processing needs a screening of each image to determine if a pixel is looking at the plume, the background, a cloud, or even a bird. This screening is based on the interpretation of the raw signals and, for instance, it sometimes fails to recognize pixels which still have in their FOV the



residual NO₂ molecules left by a past position of the plume. From our experience, the relative uncertainty on C_0 determined from a single image is generally larger than 1% (determined from the sample standard deviation). Using multiple images as explained in section 3.3 reduces this uncertainty, as C_0 is computed for each image then averaged. A 1% total relative error is achievable with a few images.

- 5 The relative instrument response non-uniformity ρ_{ij} can be obtained from a homogeneous scene (i.e. a flat field such that $I_{ij}(\lambda) = I(\lambda) \forall i, j$). In this particular case, $\rho_{ij}(\lambda) = C_{ij}(\lambda)/C(\lambda)$, where $C(\lambda)$ is the average of C_{ij} over a large number of pixels. If the flat field is built from a number of relatively homogeneous images under the assumption that their average is truly flat, then the uncertainty on the flatness participates to the error budget of $\rho_{ij}(\lambda)$ and quickly becomes the driver (signal shot noise is surpassed). This error source is a generic problem of all imaging systems but remains difficult to quantify. The only
 10 certainty is that it drops with the sample size.

The NO₂ absorption cross-section data are taken from Vandaele et al. (1998) who report a total relative uncertainty of 3% at a resolution of 2 cm⁻¹ (0.04 nm at 450 nm). Taking our coarser resolution into account (about 0.6 nm), the uncertainty drops to about 0.8%. However, the AOTF tuning curve is temperature-dependent, with a typical drift of +0.1 nm per Kelvin (Ohmachi and Uchida, 1970; Uchida, 1971). The driving electronics is currently not enslaved to a temperature sensor. The exact
 15 measurement wavelength is computed at the processing stage. Depending on the amount of wavelength drift, the uncertainty on $\sigma_{\text{NO}_2}(\lambda)$ can reach 5-10%.

The minimum relative uncertainty on the NO₂ SCD will be reached if the uncertainty on the plume transmittance T is driven by C_0 . Assuming $\sigma_T/T = 1\%$, and taking into account a 5% error on the cross-section term (with a typical value for $\sigma_{\text{NO}_2}(\lambda_s) - \sigma_{\text{NO}_2}(\lambda_w) = 2 \times 10^{-19}$), one obtains $\sigma_k = 5 \times 10^{16}$ molecules cm⁻². If one assumes less favorable conditions like
 20 a 1% uncertainty on ρ yielding $\sigma_T/T = 2\%$ and a 10% error on the cross-section, then the SCD error reaches 10¹⁷ molecules cm⁻².

4 Application to the remote sensing of NO₂ at a coal-fired power plant

The data of a spectral imager such as the NO₂ camera are more easily exploited if a number of observational requirements are satisfied. First, the camera must be placed at a location where both the plume and the background can be captured within
 25 the same image. Second, the target plume must remain optically thin in order to preserve the assumption of the Beer-Lambert extinction along a straight light path. Finally, scattered clouds behind the plume will corrupt the retrieval and should be avoided.

These three requirements were sometimes fulfilled during the second Airborne Romanian Measurements of Aerosols and Trace gases (AROMAT-2) campaign to which we participated in August 2015. The campaign aimed at joining the efforts of several European research institutes and universities to spatially and temporally characterize the emissions from two types of
 30 site: a large city (Bucharest), and point sources (large thermal power plants in the Jiu Valley, Romania). Both sites should eventually serve as validation targets for the ESA TROPOMI/S-5P mission.

The NO₂ camera was placed at a distance of 2.5km from a group of 4 stacks belonging to Turceni's power plant, the largest in Romania (330MW per turbine, 2000GWh/year total electric power generation of which more than 93% out of coal). Figure

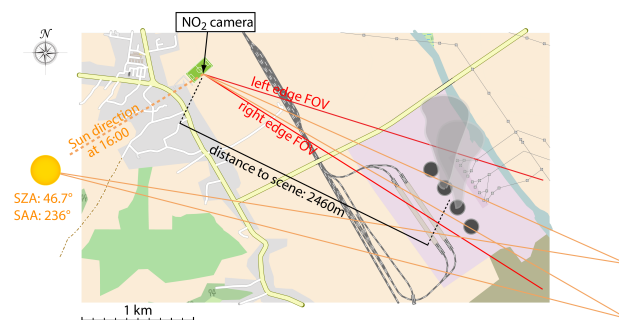


Figure 4. Observational geometry during the AROMAT-2 campaign at Turceni's power plant. The NO₂ camera was installed on a football pitch looking at the four 280m-tall stacks. The red lines delimit the camera horizontal FOV (6°). The direction of the Sun at 16:00 local time is approximately indicated, together with two rays illustrating the scattering behind the scene towards the camera. One of the rays passes through the plume, the other one passes by. [Map data from OpenStreetMap]

4 depicts the measurement geometry. Our location was 44.6792°N 23.3788°E, the line of sight (LOS) azimuth angle ranged from 113° (left edge of the image) to 119° (right edge) Eastward from North, and the LOS zenith angle ranged between 75.5° (top edge) and 81.5° (bottom edge). We only report on measurements performed on the 24th between 16:15 and 16:30 as the observational conditions were close to ideal and better illustrate the performance of the instrument.

5 4.1 Exhaust plume NO₂ SCD field

As explained in section 3.1, the 2-D NO₂ SCD field is computed from at least two spectral images recorded at wavelengths showing a significant difference of absorption cross-section. To increase the reliability of the measurements, 4 doublets of wavelengths were used: $\lambda_{w1} = 441.8$ and $\lambda_{s1} = 439.3$, $\lambda_{w2} = 446.7$ and $\lambda_{s2} = 448.1$, $\lambda_{w3} = 437.9$ and $\lambda_{s3} = 435.1$, $\lambda_{w4} = 465.8$ and $\lambda_{s4} = 463.2$. The automated acquisition system was in charge of synchronizing the driving of the AOTF with the image acquisition. A nominal acquisition sequence started by setting the appropriate RF signal for the AOTF to filter at λ_{w1} , open the CCD shutter for 0.5s, readout the image and repeat these operations for the 7 other wavelengths. After completion of the nominal sequence, a picture with the AOTF turned off is taken and the nominal sequence is resumed. The dwell time between the closing of the shutter and its re-opening was 1.3 s. In the plane of the stacks, the image footprint spans an area of $250 \times 250 \text{ m}^2$ with a 50 cm sampling.

15 The data analysis revealed that the images from the 2nd and 4th doublets were the less noisy, because of a larger natural radiance and sensor sensitivity compared to the wavelengths of doublets 1 and 3. Also, due to the plume displacement over time (wind), and the presence of moving and changing inhomogeneities across the plume (puffs, turbulent eddies), it was necessary to perform time averaging (section 3.3). Indeed, the 1.3 second between two consecutive images is already a long time for features moving at a typical 5 m s^{-1} speed (corresponding to 10 pixels per second).

20 Figure 5 shows the NO₂ SCD field retrieved from the averaging of images taken at λ_{w2} , λ_{s2} , λ_{w4} and λ_{s4} (12 of each) using the method described in Section 3.3. For each wavelength, the background signal C_0 was determined from image areas

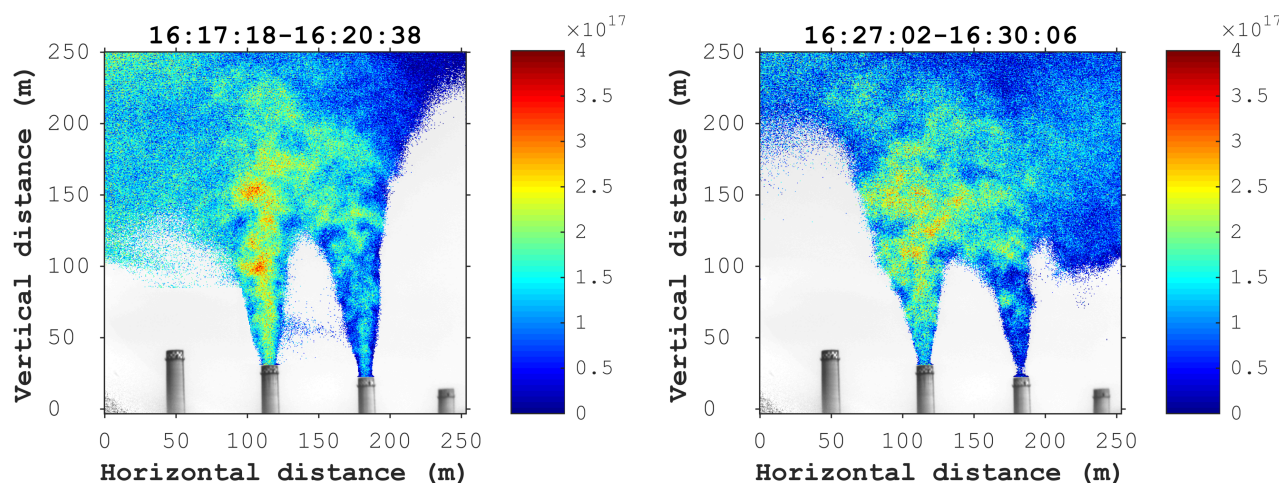


Figure 5. Sample NO_2 SCD field obtained from the averaging of images acquired at $\lambda_{w2} = 446.7\text{nm}$, $\lambda_{s2} = 448.1\text{nm}$, $\lambda_{w4} = 465.8\text{nm}$ and $\lambda_{s4} = 463.2\text{nm}$ (12 of each). The colorscale shows the plume NO_2 SCD in molecules cm^{-2} . The x- and y-axis show the image dimensions in the scene plane, while the title gives the time span (local time).

untouched by the plume. The relative error is about 0.5% (estimated from the standard deviation σ_{C_0} of the pixels sample yielding C_0). Within this precision, no variation of C_0 across the FOV could be significantly detected. The reason is the relatively small FOV of the camera (about 6°) combined with a high Sun at the time of the measurements (making the scene illumination quite homogeneous). In Fig. 5, the background grayscale image is the mean image at λ_{w4} , whereas the pixels where the SCD is computed were selected based on the criterium $C_{ij} < C_0 - 2\sigma_{C_0}$. Investigating the random fluctuations observed in various areas of the SCD field, one can estimate the detection limit to about 5×10^{16} molecules cm^{-2} .

4.2 NO_2 emission fluxes and synergies with SO_2 cameras

The capability of resolving the NO_2 SCD field with a high spatial and temporal resolution provides new possibilities for the understanding of the plume chemistry. Coal combustion processes yielding the formation of nitrogen and sulfur species are well-known (Flagan and Seinfeld, 1988), and several reactive plume models can simulate the transport, formation and removal of these species over different scales. These models are generally validated by in-situ air sampling at distances of several kilometres downwind (see for instance Chowdhury et al. (2015)). Very few experiments attempted to characterize the reactive content of the early plume, where the reactions are still governed by the combustion products (Hewitt, 2001). In most cases, a DOAS scanning system was used (Lee et al., 2014, 2009; Lohberger et al., 2004). The same technique was also used for SO_2 , but to a lesser extent since the introduction of filter-based SO_2 cameras (Smekens et al., 2015). Recently, imaging Fourier-transform spectroscopy (IFTS) demonstrated capability for the measurement of a number of mid-infrared emitting species such as CO_2 and SO_2 (Gross et al., 2010). However, NO but not NO_2 , can be retrieved with this technique.

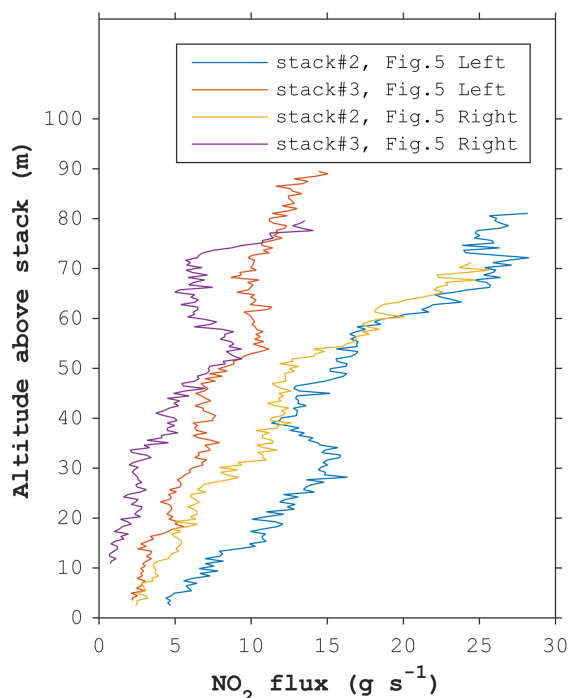


Figure 6. NO₂ flux computed through the plume horizontal cross-section as a function of altitude. Stacks height is 280m. A symmetric Gaussian dispersion is assumed up to the region of apparent intersection of the two plumes.

An undisputed advantage of imaging systems with high temporal resolution is their ability to track the displacement of remarkable features from one image to another. We used the complete time series of spectral images (50 sequences of 8 spectral images at a rate of 0.5 Hz) to determine the vertical speed of the plume. This was done by tracking signal features created by local increase or decrease of the NO₂ concentration. On average, a vertical speed of $4.8 \pm 0.5 \text{ m s}^{-1}$ was observed.

- 5 Furthermore, assuming a Gaussian dispersion of the plume, one can infer a circular cross-section from the apparent width of the plume at each detector row (i.e. every 50 cm above the stack outlet). As a result, a profile of emission flux (in g s^{-1}) can be drawn. Figure 6 shows the NO₂ emission flux as a function of altitude up to a height above which the two plumes cannot be discriminated anymore. The fluxes were calculated from the two SCD maps of Fig. 5, and both stacks. The increase is the result of the conversion of NO into NO₂ mainly by the reactions $2\text{NO} + \text{O}_2 \rightarrow 2\text{NO}_2$, and $\text{NO} + \text{HO}_2 \rightarrow \text{NO}_2 + \text{OH}$ (Flagan and Seinfeld, 1988; Miller and Bowman, 1989), even if these processes are balanced by the photodissociation of NO₂ as soon as it reaches open air under day light ($\text{NO}_2 + h\nu \rightarrow \text{NO} + \text{O}$). Qualitatively, these results agree well with the increase reported by Lee et al. (2009) in a study of the rate of increase of NO₂ above power plant stacks. The analysis of Fig. 6 reveals that
- 10 within the method approximations, the NO₂ concentration in the plume increases at a rate ranging from 0.75 to 1.25 g s^{-1} (9.8×10^{21} - $1.6 \times 10^{22} \text{ molecules s}^{-1}$) on average for the first 20 seconds.



The knowledge of the spatial distribution of NO_2 can also prove useful to correct measurements marked by interference from NO_2 . A good example is with SO_2 cameras where the SO_2 SCD field is retrieved by comparing the plume transmittance around 310 and 330 nm. In this range, NO_2 is also absorbing and its cross-section roughly doubles from 310 to 330 nm. Therefore, if both molecules are present in the plume, the SO_2 camera alone cannot disentangle their respective signature. So far, this interference has been overlooked in SO_2 camera validation exercises (Smekens et al., 2015; Kern et al., 2010). In the case of the plumes shown in Fig. 5 for instance, a SO_2 camera such as the one used by Smekens et al. (2015) would observe a $\Delta\tau_{\text{NO}_2} = 0.04$ when the NO_2 SCD reaches 3×10^{17} molecules cm^{-2} . This variation of optical thickness corresponds to a SO_2 SCD of about 1.6×10^{17} molecules cm^{-2} , which is twice the detection limit reported in Smekens et al. (2015). Clearly, the bias would increase with higher concentrations of NO_2 . Taking advantage of the similar spatial resolution of both instruments, the NO_2 camera can provide a complete correction map for the SO_2 data.

5 Conclusions

We have described a new passive atmospheric remote sensing instrument for the measurement of NO_2 slant column densities (SCDs) above strong sources. It is based on an acousto-optical tunable filter (AOTF) which offers a sufficient acceptance angle to be placed in an imaging system, and the necessary resolution for taking advantage of the fine structures of the NO_2 absorption cross-section. The AOTF is electrically driven, such that fast synchronized acquisitions of spectral images are possible.

The measurement principle is similar to the filter-based SO_2 camera: SCDs are retrieved from at least two spectral images where absorption by the target molecule is significantly different. Wavelengths are picked in the range 440–470 nm. Thanks to its higher spectral resolution, the AOTF-based NO_2 camera can perform its measurements within a few nanometres. This makes the sensitivity to aerosols negligibly small.

A mathematical frame has been developed, and the different sources of error have been addressed. In applications focusing on relatively high spatio-temporal resolution, the NO_2 SCD detection limit is about 5×10^{16} molecules cm^{-2} . Different measurement geometries offering longer staring time or more stable targets would yield a lower limit.

The NO_2 camera was successfully tested during the AROMAT-2 campaign where measurements of NO_2 SCD fields above the flue gas stacks of a coal-fired power plant were performed with a temporal resolution of 3 minutes and a spatial sampling of 50 cm (for a complete scene of $250 \times 250 \text{ m}^2$). Values up to 4×10^{17} molecules cm^{-2} were observed. The quality of the data allowed to clearly identify the conversion process from NO to NO_2 in the early plume, providing quantitative information on the plume dynamic chemistry. In another example of application, the measurements were used to show how the knowledge of the high resolution NO_2 field can help to correct SO_2 camera data. If overlooked, the interfering absorption of NO_2 can yield a significant bias in the retrieved SO_2 SCDs. Other applications range from emission monitoring to volcanic plume chemistry.

While the concept is mature, a number of improvement directions are still being investigated. The most promising ones are the implementation of a temperature feedback loop to reduce the uncertainty on the filtered wavelength, and the replacement of the CCD by a CMOS in order to reduce the cooling needs and increase the temporal resolution of the measurements.



Author contributions. E. Dekemper developed the NO₂ camera measurement principle, led the characterization and the participation to the AROMAT-2 campaign, and processed the data. B. Van Opstal and J. Vanhamel developed the acquisition software and the AOTF driving electronics, and participated to the campaign. D. Fussen is at the origin of the instrument concept and supported its development in the frame of the ALTIUS project. The authors declare that they have no conflict of interest.

- 5 *Acknowledgements.* This work was funded under PRODEX contract 4000110400. Participation to the AROMAT-2 campaign was funded under ESA contract 4000113511. The authors would like to thank Alexis Merlaud for inviting them to participate to the AROMAT-2 campaign. E. Dekemper would like to thank Kerstin Stebel for the interesting discussions on SO₂ cameras, and Vitaly Voloshinov for his support in all AOTF-related matters.



References

- Bluth, G. J. S., Shannon, J. M., Watson, I. M., Prata, A. J., and Realmuto, V. J.: Development of an ultra-violet digital camera for volcanic SO₂ imaging, *J. Volcanol. Geotherm. Res.*, 161, 47–56, doi:10.1016/j.jvolgeores.2006.11.004, <http://www.sciencedirect.com/science/article/pii/S0377027306003957>, 2007.
- 5 Chang, I. C.: Noncollinear acousto-optic filter with large angular aperture, *Appl. Phys. Lett.*, 25, 370, doi:10.1063/1.1655512, <http://adsabs.harvard.edu/abs/1974ApPhL...25..370C><http://scitation.aip.org/content/aip/journal/apl/25/7/10.1063/1.1655512>, 1974.
- Chowdhury, B., Karamchandani, P., Sykes, R., Henn, D., and Knipping, E.: Reactive puff model SCICHEM: Model enhancements and performance studies, *Atmos. Environ.*, 117, 242–258, doi:10.1016/j.atmosenv.2015.07.012, 2015.
- Dekemper, E., Loodts, N., Van Opstal, B., Maes, J., Vanhellemont, F., Mateshvili, N., Franssens, G., Pieroux, D., Bingen, C., Robert, C., De Vos, L., Aballea, L., and Fussen, D.: Tunable acousto-optic spectral imager for atmospheric composition measurements in the visible spectral domain, *Appl. Opt.*, 51, 6259, doi:10.1364/AO.51.006259, <https://www.osapublishing.org/ao/abstract.cfm?uri=ao-51-25-6259>{&}origin=search{#}Abstract, 2012.
- Flagan, R. C. and Seinfeld, J. H.: *Fundamentals of Air Pollution Engineering*, Prentice Hall, Englewood Cliffs, <http://resolver.caltech.edu/CaltechBOOK:1988.001>, 1988.
- 15 Gross, K. C., Bradley, K. C., and Perram, G. P.: Remote identification and quantification of industrial smokestack effluents via imaging fourier-transform spectroscopy, *Environ. Sci. Technol.*, 44, 9390–9397, doi:10.1021/es101823z, 2010.
- Heue, K.-P., Wagner, T., Broccardo, S. P., Walter, D., Piketh, S. J., Ross, K. E., Beirle, S., and Platt, U.: Direct observation of two dimensional trace gas distributions with an airborne Imaging DOAS instrument, *Atmos. Chem. Phys.*, 8, 6707–6717, doi:10.5194/acp-8-6707-2008, <http://www.atmos-chem-phys.net/8/6707/2008/>, 2008.
- 20 Hewitt, C. N.: The atmospheric chemistry of sulphur and nitrogen in power station plumes, *Atmos. Environ.*, 35, 1155–1170, doi:10.1016/S1474-8177(02)80012-2, 2001.
- Kern, C., Kick, F., Lübcke, P., Vogel, L., Wöhrbach, M., and Platt, U.: Theoretical description of functionality, applications, and limitations of SO₂ cameras for the remote sensing of volcanic plumes, *Atmos. Meas. Tech.*, 3, 733–749, doi:10.5194/amt-3-733-2010, <http://www.atmos-meas-tech.net/3/733/2010/>, 2010.
- 25 Lee, H., Kim, Y. J., and Lee, C.: Estimation of the rate of increase in nitrogen dioxide concentrations from power plant stacks using an imaging-DOAS, *Environ. Monit. Assess.*, 152, 61–70, doi:10.1007/s10661-008-0296-4, 2009.
- Lee, H., Ryu, J., Jeong, U., Noh, Y., Shin, S. K., Hong, H., and Kwon, S.: Improvement in plume dispersion formulas for stack emissions using ground-based imaging-DOAS data, *Bull. Korean Chem. Soc.*, 35, 3427–3432, doi:10.5012/bkcs.2014.35.12.3427, 2014.
- Lohberger, F., Hönninger, G., and Platt, U.: Ground-based imaging differential optical absorption spectroscopy of atmospheric gases, *Appl. Opt.*, 43, 4711, doi:10.1364/AO.43.004711, <http://www.osapublishing.org/viewmedia.cfm?uri=ao-43-24-4711>{&}seq=0{&}html=true, 2004.
- 30 Lübcke, P., Bobrowski, N., Illing, S., Kern, C., Alvarez Nieves, J. M., Vogel, L., Zielcke, J., Delgado Granados, H., and Platt, U.: On the absolute calibration of SO₂ cameras, *Atmos. Meas. Tech.*, 6, 677–696, doi:10.5194/amt-6-677-2013, <http://www.atmos-meas-tech.net/6/677/2013/amt-6-677-2013.html><http://www.atmos-meas-tech.net/6/677/2013/amt-6-677-2013.pdf>, 2013.
- 35 Miller, J. A. and Bowman, C. T.: Mechanism and modeling of nitrogen chemistry in combustion, *Prog. Energy Combust. Sci.*, 15, 287–338, doi:10.1016/0360-1285(89)90017-8, <http://www.sciencedirect.com/science/article/pii/0360128589900178>, 1989.



- Mori, T. and Burton, M.: The SO₂ camera: A simple, fast and cheap method for ground-based imaging of SO₂ in volcanic plumes, *Geophys. Res. Lett.*, 33, L24 804, doi:10.1029/2006GL027916, <http://doi.wiley.com/10.1029/2006GL027916>, 2006.
- Ohmachi, Y. and Uchida, N.: Temperature Dependence of Elastic, Dielectric, and Piezoelectric Constants in TeO₂ Single Crystals, *J. Appl. Phys.*, 41, 2307–2311, doi:10.1063/1.1659223, <http://scitation.aip.org/content/aip/journal/jap/41/6/10.1063/1.1659223>, 1970.
- 5 Platt, U., Lübcke, P., Kuhn, J., Bobrowski, N., Prata, F., Burton, M., and Kern, C.: Quantitative imaging of volcanic plumes - Results, needs, and future trends, *J. Volcanol. Geotherm. Res.*, 300, 7–21, doi:10.1016/j.jvolgeores.2014.10.006, <http://dx.doi.org/10.1016/j.jvolgeores.2014.10.006>, 2014.
- Seinfeld, J. H. and Pandis, S. N.: *Atmospheric chemistry and physics*, Wiley, Hoboken, New Jersey, 2nd edn., 2006.
- Smekens, J.-F., Burton, M. R., and Clarke, A. B.: Validation of the SO₂ camera for high temporal and spatial resolution monitoring of SO₂
 10 emissions, *J. Volcanol. Geotherm. Res.*, 300, 37–47, doi:10.1016/j.jvolgeores.2014.10.014, <http://www.sciencedirect.com/science/article/pii/S0377027314003126>, 2015.
- Uchida, N.: Optical Properties of Single-Crystal Paratellurite (TeO₂), *Phys. Rev. B*, 4, 3736–3745, doi:10.1103/PhysRevB.4.3736, <http://link.aps.org/doi/10.1103/PhysRevB.4.3736><http://journals.aps.org/prb/abstract/10.1103/PhysRevB.4.3736>, 1971.
- Vandaele, A. C., Hermans, C., Simon, P. C., Carleer, M., Colin, R., Fally, S., Mérienne, M. F., Jenouvrier, A., and Coquart, B.: Measurements
 15 of the NO₂ absorption cross-section from 42 000 cm⁻¹ to 10 000 cm⁻¹ (238–1000 nm) at 220 K and 294 K, *J. Quant. Spectrosc. Radiat. Transf.*, 59, 171–184, doi:10.1016/S0022-4073(97)00168-4, <http://www.sciencedirect.com/science/article/pii/S0022407397001684>, 1998.
- Voloshinov, V. B., Yushkov, K. B., and Linde, B. B. J.: Improvement in performance of a TeO₂ acousto-optic imaging spectrometer, *J. Opt. A Pure Appl. Opt.*, 9, 341–347, doi:10.1088/1464-4258/9/4/006, <http://iopscience.iop.org/1464-4258/9/4/006><http://www.misis.ru/Portals/0/Download/Press/2011/VoloshinovYushkovLinde07.pdf>, 2007.